DESIGNING A THEORETICAL MODEL FOR DETERMING IONOSPHERIC CURRENT DENSITIES

by

ELIA P. REICHARDT

A THESIS

Presented to the Department of Physics
and the Robert D. Clark Honors College
in partial fulfillment of the requirements for the degree of
Bachelor of Science

May 2026

An Abstract of the Thesis of

Elia P. Reichardt for the degree of Bachelor of Science
in the Department of Physics to be taken June 2026

Title: Designing a Theoretical Model for Determing Ionospheric Current Densities

Approved: *Carol S. Paty, PhD, Professor of Earth Sciences*
Primary Thesis Advisor

While significant effort has been made in recent years regarding the modeling of the upper atmosphere, much of this modeling focuses on large-scale and long-term events and neglects the vertical structure of the E-region. To address this deficiency, we describe the development and function of the Localized Ionospheric Dynamo Region Model (LIDRM). The LIDRM is a theoretical model which is capable of providing altitude profiles for a number of different ionospheric parameters, including horizontal current density, Hall and Pedersen conductivity, and auroral electron ionization. Comparing our model to Incoherent Scatter Radar (ISR) data from the EISCAT radar, we find good agreement regarding electric current densities and Hall and Pedersen conductivities. We also attempt to amend the incorrect results found in a similar paper and provide corrections to the literature.

Table of Contents

Section I: Introduction 5
Section I.1: The Atmosphere & Ionosphere 5
Section I.2: The Ionospheric Dynamo Region 8
Section I.3: Dynamo Current Flow 11
Section II: Motivations 14
Section II.1: Research Importance 14
Section II.2: Current knowledge gaps 15
Section II.3: Sounding Rocket Assistance 17
Section II.4: Model Necessity 19
Section III: Model Design 20
Section III.1 Background 20
Section III.2: Model Setup 21
Section III.3: Precipitation Modelling 22
Section III.4: Current Density Profiles 24
Section IV: Results 28
Section IV.1: Dynamo Region Modeling 28
Section IV.2: Previous South Atlantic Dynamo Measurements 30
Section IV.3 Equatorial and mid-latitude current density forcing 34
Section IV.5: Polar current densities 40
Section V: Conclusions 44
Section V.1: Future Work 44
Bibliography 47

List of Figures

Fig. 1: Overview of Upper Atmosphere 6
Fig. 2: Dynamo Current Generation 8
Fig. 3: Dynamo region above Tromsø, Norway 28
Fig. 4: Dynamo region above the South Atlantic Anomaly 30
Fig. 5: Dynamo region above area of strong magnetic field 31
Fig. 6: Figure 2 from Xi et al., 2023 32
Fig. 7: Average current due to dynamo forcing above Millstone Hill, MA 35
Fig. 8: Average current due to dynamo forcing above Thumba, India 36
Fig. 9: Electron density at 2:00 UTC above Tromsø EISCAT ISR during substorm 38
Fig. 10: Electron density at 5:00 UTC above Tromsø EISCAT ISR during substorm 39
Fig. 11: Midnight (2:00 UTC) vs. morning (5:00 UTC) electron densities 40
Fig. 12: Figure 2 from Sato et al., 1994 41
Fig. 13: LIDRM output for current density during April 10 substorm 42
Fig. 14: Hall and Pedersen conductivity 43

Section I: Introduction

This thesis will describe the development of our new ionospheric model, which, for the first time, provides a full vertical profile of ionospheric current density. This first section will provide context for those unfamiliar with the subject to understand the scientific reasoning which underlines our modelling work.

Section I.1: The Atmosphere & Ionosphere

The most common definition for the beginning of outer space is the Karmán line–at 100 kilometers above sea level of the Earth. In reality, however, it is impossible to define an altitude which the atmosphere lies below and space lies above. The atmosphere decreases in density as altitude increases–even at 400 kilometers altitude, the International Space Station still experiences atmospheric drag. The lower the altitude, the greater the drag–so much so that stable orbits are virtually impossible below 200 km (in-situ satellite observations have only been performed below this three times, with the last occurrence in 1981 (Sarris et al., 2023)). While the atmosphere here may be too thick for satellites, it is far too thin for flying craft. The maximum altitude attainable from below is via weather balloon, but these cap out at around 50 kilometers in height. The study of the region between 50 and 200 kilometers, consequently, is highly difficult. As a result, it has often been overlooked by researchers and been given the humorous monicker “ignorosphere”.

The Earths’ atmosphere is composed of five layers, with boundaries defined by peaks and troughs in temperature. The densest part of the atmosphere is the troposphere (0-12km)–then above this, in order, there is the stratosphere (12-50km), the mesosphere (50-85km) the thermosphere (85-700km), and finally the exosphere (700+ km). Figure 1 provides a sense of scale this, with relevant processes depicted.

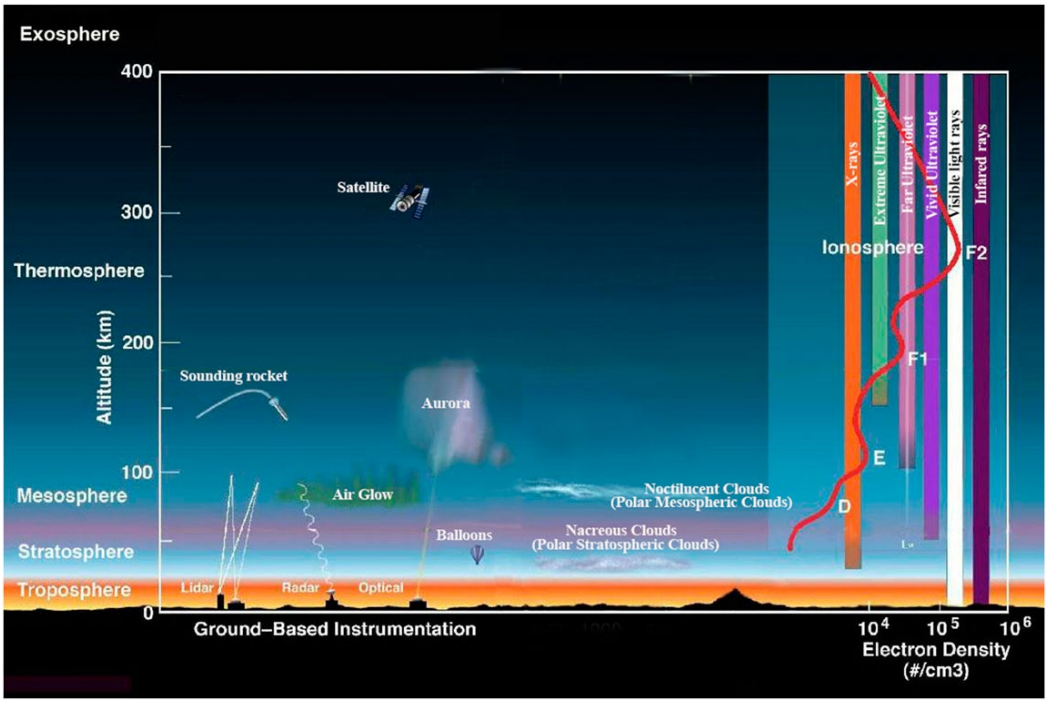


Fig. 1: Overview of Upper Atmosphere

Overview of the different layers of the atmosphere, with relevant phenomena depicted. From NASA, 2019.

While the atmosphere is continuous, it is not homogenous. Above the stratosphere, the levels of atmospheric ozone decrease substantially. Ozone is an excellent absorber of solar UV radiation–radiation which is energetic enough to remove electrons from neutral particles, through a process known as ionization. Ionization creates negatively charged free electrons, as well as positively charged ions. At altitudes just above the stratosphere, the density is high enough such that collisions between particles are frequent, and so charged particles recombine before a stable population can be achieved. However, as altitude increases, so does ionization rates, while the rate at which charged particles are lost (the recombination rate), falls as density does. At around 100 kilometers, charged species are able to maintain a stable population–a gas of charged particles forms a plasma, which is known as the ionosphere.

The density of the ionosphere is determined by a balance between the ionization and recombination rates. The relationship between these two quantities determines the ionospheric structure, which is typically divided into three regions: D, E, and F. The D-region extends from 60-90 km, though it is generally very sparse during the day, and completely disappears at night due to the lack of solar UV radiation. Above this is the E-region, from 90-150 km. Most of the ionization in the E-region is a consequence of longer wavelength UV (90 nm), although energetic particle precipitation (EPP) plays a larger role at high latitudes (Baumjohann & Treumann, 2022). The E-region is well-defined in the presence of solar UV and is usually prominent enough to be detectable at night. Above the E-region is the F-region, which remains consistently ionized.

It is important to remember that the ionosphere does not replace the neutral atmosphere– the ionosphere is simply the term coined for the collective population of charged particles in the upper atmosphere. Ionospheric particles make up a very small (roughly 1 in 10^6 at 100 km) fraction of the overall upper atmosphere. The ionosphere is treated as a separate fluid because the charged particles move together collectively via electromagnetic forces, in contrast to the solely collisional physics which govern the motion of neutrals. However, because charged particles interact directly with electromagnetic fields, their effects are far more wide-reaching that the movements of the neutral particles. One of the factors contributing to this is the connection between the ionosphere and the magnetosphere. At high latitudes, the interaction between the solar wind and magnetosphere generates an electric field which is mapped along magnetic field lines and creates strong plasma flow in the F-region (Schunk & Nagy, 2000). In the E-region, however, plasma flows are mostly dominated by a different mechanism, which will be discussed in the following section.

Section I.2: The Ionospheric Dynamo Region

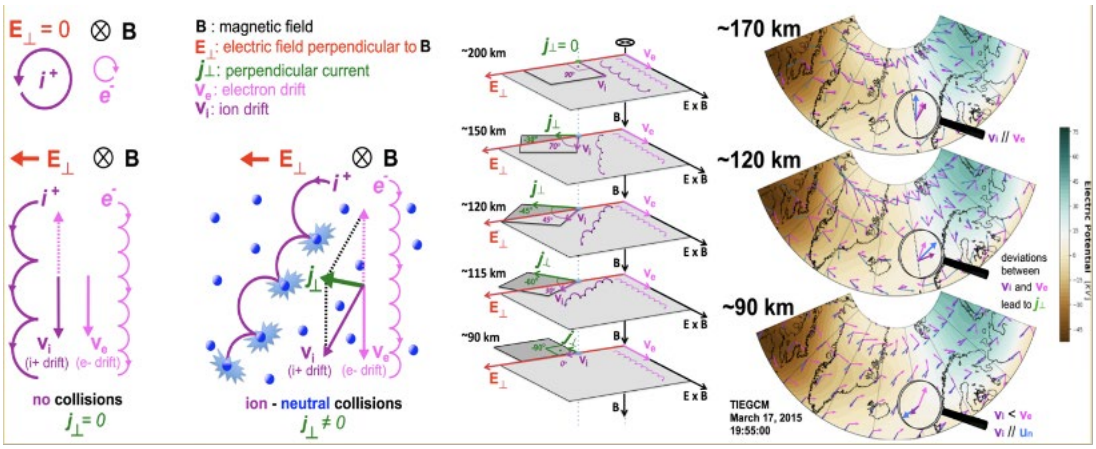


Fig. 2: Dynamo Current Generation

An overview of how electric currents are generated in the ionosphere. Ions collide with neutral particles at a far higher rate than electrons, causing the ions to drift in the direction of the neutral particle motion and the driving electric field. On the right, the change in current with altitude is depicted. From Sarris et al., 2023.

While the ionosphere and the neutral atmosphere are often treated as separate entities, coupling between the two forms a major component of upper atmospheric dynamics. Additionally, the ionospheric plasma is not made of homogenous particles–ions and electrons will both act differently given their differences in mass and charge. The differential motion of ions and electrons has a significant effect in determining the structure and properties of the ionosphere.

In the presence of a magnetic field, the Lorentz force causes charged particles to circle around magnetic field lines. The direction of motion is determined by the charge of the particles involved–positive charges orbit counterclockwise, and negative charges orbit clockwise. The gyrofrequency ω, or rate at which a particle with charge q and mass m orbits in the presence of a magnetic field $\vec{B}$ is given by the following equation:

$$\omega = \frac{q\vec{B}}{m} \tag{1}$$

Because the magnetic field vector is dominated by the geomagnetic field of the Earth, two particles close together will experience roughly the same magnetic field strength. Therefore, the only difference in gyrofrequency will be caused by the particles charge and mass. All electrons have the same charge, and while ions do vary in their level of ionization, the magnitude of the charge is insignificant given the massive difference in mass between ions and electrons. Therefore, gyrofrequency is mostly determined by the mass of the particles in question: in the ionosphere, electrons have a gyrofrequency on the order of 10^7 s^{-1}, whereas the ion gyrofrequency is typically on the order of 10^2 s^{-1}.

In a constant magnetic field, charged particles will simply remain circling in their orbits. However, this is rarely the case in the ionosphere. As the Earth rotates, so too does its magnetic field. Via Faraday's law, this movement generates an induced electric field perpendicular to the incumbent magnetic field. What occurs can be observed in figure 2: ions are accelerated in the direction of the electric field, and so when orbiting this direction, they are sped up. When their rotation moves them so that they are travelling against the electric field, they are then slowed down. This creates a sort of "half-circle jump", ultimately pushing the ions in a direction perpendicular to both the electric and magnetic fields. While electrons are decelerated in the direction of an electric field, the fact that they rotate in the opposite direction of ions means that they end up moving in the same direction as the ions. This effect is known as $\vec{E} \times \vec{B}$ ("E-cross-B") drift, and it is a significant driver of plasma motion in the ionosphere. In the F-region and throughout the magnetosphere, $\vec{E} \times \vec{B}$ drift is a major factor in determining plasma drift.

However, plasma motion due solely to $\vec{E} \times \vec{B}$ drift is incapable of producing electric currents. As the ions and electrons end up travelling the same direction, the motion of positive and negative charges cancels each other out. In the F-region and above, $\vec{E} \times \vec{B}$ drift serves as a

good approximation of plasma motion. At lower altitudes, however, the density of neutral particles is much higher. The rate at which charged particles collide with neutral particles is quantified by the ion-neutral and electron-neutral collision frequencies. The relationship between the collision frequency and the gyrofrequency determines the characteristics of the plasma flow. In the F-region, the gyrofrequencies of both electrons and ions are much greater than their collision frequency–thus, a charged particle will on average complete multiple rotations before a collision with a neutral particle, and plasma flows are determined by the $\vec{E} \times \vec{B}$ drift. Similarly, in the lower atmosphere, the few free charged particles which do exist have a much greater neutral collision frequency than they do gyrofrequency, and so charged particles are pushed along with the flow of the neutrals.

Between about 70 and 130 km, however, an interesting dynamic forms. Electrons, on account of their smaller mass, have a higher gyrofrequency than the ions. They therefore move according to $\vec{E} \times \vec{B}$ drift. Ions, on the other hand, have a higher collision frequency than they do gyrofrequency. In turn, ion motion is mostly determined by the motion of the surrounding neutrals. This effect is known as the ionospheric dynamo, and its existence defines the ionospheric dynamo region (Yamazaki & Maute, 2017). The upper bound of the dynamo region is where the ion-neutral collision frequency is equal to the ion gyrofrequency, and the lower bound is where the electron-neutral collision frequency is equal to the electron gyrofrequency. Crucially, it is the dynamo effect which is capable of producing ionospheric currents, as the motions of ions and electrons are decoupled from one another, allowing for a net flow of charge to occur.

Section I.3: Dynamo Current Flow

Just as the ionosphere is heterogenous in structure, so is the current flow which dynamo action creates. In the ionosphere, currents are defined by their direction of motion in relation to the geomagnetic and electric field. Pedersen currents flow in the direction of the magnetic field, Hall currents flow perpendicular to the magnetic and electric field, and field-aligned currents (FACs, also called Birkeland currents) flow along geomagnetic field lines. The ability of current to flow in a given direction is moderated by the conductivity along said direction. Conductivity along magnetic field lines is very high, and therefore field aligned currents provide a pathway for plasma to flow from the ionosphere to the magnetosphere. FACs are dominant and mostly limited to the polar regions, as plasma flows along the dipolar geomagnetic field. Hall and Pedersen currents, meanwhile, flow throughout the ionosphere, and are more dependent on altitude than latitude. Hall conductivity typically maximizes around 100 km, as ion motion is impeded significantly by a higher neutral density. The Hall current is then mostly carried by the free electrons. Pedersen conductivity peaks around 130 km, as ions are less impacted by dynamo forcing that at lower altitudes, and so the driving electric field is a greater component of their motion (Baumjohann & Treumann, 2022, Sarris et al., 2023). Hall and Pedersen currents play a major role in determining the structure of the global current system, providing channels for plasma flow. They also serve an important role in determining the energy budget of the upper atmosphere, as Joule heating due to current flow through the resistive neutrals is a major source of upper atmospheric heating. (Palmroth et al., 2021).

The strength of dynamo currents is highly influenced by upper atmospheric winds. These winds are primarily generated via energy transport from atmospheric waves, which are generated in the lower atmosphere and then propagate upwards. Atmospheric waves “break” in the upper

atmosphere, similar to the way ocean waves crest on a beach, transferring energy generated in the lower atmosphere to the dynamo region. Atmospheric waves span a huge volume of spatial scales, with the very largest able to oscillate throughout entire hemispheres.

Among the most prominent of these oscillations are atmospheric tides. Tides oscillate with principal frequencies of 24h (diurnal) and 12h (semidiurnal), although 8h (terdiurnal) and 12.4h (lunar) are also evident. The strongest tides are created by solar heating of the lower atmosphere, causing temperature and pressure imbalances which propagate into the upper atmosphere (for seminal work, see Chapman & Lindzen, 1969). Recent study suggests that non-migratory tides (tides which move relative to the sun from the point of view of a stationary observer on the Earth's surface) play a critical role in determining material circulation in the dynamo region. Interactions between the diurnal westward 1 oscillation (DW1) and diurnal eastward 3 oscillation (DE3, with numbers corresponding to the wave number) serve as almost permanent features in the upper atmosphere and serve commanding roles in upper atmospheric dynamics (for a more detailed analysis, see Vincent, 2015).

Another type of important atmospheric wave are gravity waves (not to be confused with gravitational waves), which recent modelling has suggested also play a keystone role in moderating the activity of the upper atmosphere. The term gravity waves refer to any wave where gravity acts as a restoring force. They are generated by a plethora of sources, including, but not limited to, orography (e.g., mountains), convection, wind shear, atmospheric wave interactions, earthquakes, and tsunamis (Fritts & Alexander, 2003). As they propagate upwards, decreasing atmospheric density causes gravity wave amplitude to increase exponentially, where they then break and transfer their energy. Consequently, gravity waves provide a significant contribution to the energy budget of the dynamo region. Simulations show that the total daily

energy flux provided by gravity waves is similar in magnitude to the flux provided by Joule heating (100-150 GW), even though this simulation likely significantly underestimates the energy flux from gravity waves. (Palmroth et al., 2021). Despite their importance, gravity waves are still poorly accounted for in climate models. They are highly variable and vary over many spatial scales, making their quantification difficult. As a result, gravity waves constitute a key gap in our understanding of the upper atmosphere. They have been linked to the creation of travelling ionospheric disturbances (TIDs), which form as propagating waves in ionospheric plasma. TIDs and other perturbations create variations in local ionospheric conditions. In turn, these variations can influence other aspects of the upper atmospheric system, such as energy and momentum transport (see Liu, 2016 and Palmroth et al., 2021 for a more comprehensive description).

By developing a model of the upper atmosphere which uses empirical data as the background, we are able to observe many of the yet-to-be quantified effects of atmospheric waves. Greater understanding and quantification of phenomena such as these is necessary to expand scientific knowledge of the upper atmosphere, which this thesis seeks to achieve. In the following sections, we will explain the purpose and function of the ionospheric model which we have created. Section II will explain our scientific motivations regarding this model's design. Section III will explain the theoretical basis of our model. Section IV will discuss model results, and section V will discuss conclusions.

Section II: Motivations

Section II will discuss the centrals scientific objectives which motivated the design of this model, in addition to justification as to its importance and relevance.

Section II.1: Research Importance

In recent years, researchers have concluded that accurate models of the Earth system can only be achieved through an understanding of the Earth system as a whole. Better modelling of the upper atmosphere will not just be used to advance scientific understanding but are also important for a variety of economic and societal reasons. Improved predictions of satellite drag in low Earth orbit, for instance, will facilitate more refined mission planning, as mission planners can better optimize the amount of propellant needed for stationkeeping. They may also be used for understanding the danger posed by orbital debris. Better modelling efforts will also facilitate a better understanding of the effects of high geomagnetic activity on orbiting spacecraft. Doing so will allow satellites to achieve greater reliability, longevity, and capability. Back on Earth, understanding the effects of particle precipitation (among other phenomena) on atmospheric chemistry allows for greater comprehension on important climate related issues, such as ozone production.

The ionosphere's most important impacts come from its electromagnetic interference. Electron density fluctuations can cause aberrations in GPS, radio, and telecommunications signals. Improved characterization of upper atmospheric and ionospheric dynamics is necessary to further mitigate these impacts. High solar and geomagnetic activity can further worsen these issues, leading to GPS failure and radio blackouts. In addition, strong solar and magnetospheric activity can induce ionospheric currents strong enough to cause significant issues for ground based electrical infrastructure. So-called geomagnetically induced currents (GICs) can cause

issues for infrastructure such as transmission lines and power transformers (for a detailed analysis of GICs, see Pulkkinen et al., 2017). Low intensity GIC variations are capable of introducing harmful harmonic components to transmission lines, which can create hotspots in infrastructure and increase transformer power consumption. Over time, this can lead to component failure, increasing overall maintenance costs (for more information, see sources listed in §2.2 in ESA, 2022).

Perhaps the biggest danger from solar and magnetospheric activity comes from the threat of major solar flares. In 1989, a geomagnetic storm completely blacked out the electrical systems of Hydro-Quebec for hours, causing massive blackouts which lead to over $13 million in damages (Bolduc, 2002). In 1859, the Earth was affected by an incredibly strong geomagnetic event, rendering telegraphs in Europe and North American inoperable for days, and creating aurora visible as far south as Panama. Named the Carrington, event, it is estimated an event of similar magnitude occurring today could cause damages ranging from $0.6-$2.3 trillion ($0.8-$3.6 in 2025) in the United States alone (Lloyd's of London, 2017). While such events are thankfully uncommon, they are not remarkably so, and it is necessary to prepare for one in the near future. A greater understanding of GICs and their subsequent effect on the magnetosphere and ionosphere will allow us to better prepare for future geomagnetic events, allowing us to predict the areas which are mostly likely to be affected.

Section II.2: Current knowledge gaps

The past few years have seen significant advances made in the accuracy and resolution of upper atmospheric and ionospheric models. The current flagship ionospheric model is the US National Science Foundation National Center for Atmospheric Research (NSF NCAR)'s thermosphere-ionosphere-electrodynamics general circulation model (TIEGCM). The recently

released 3.0 version is capable of a maximum horizontal resolution of 0.625º, with a maximum vertical resolution of 1/16 scale height (roughly 0.5 km–see Wu et al., 2025). This represents a significant improvement from previous versions of TIEGCM, as it provides far greater resolution than previous models (having a 2.5º resolution). TIEGCM is capable of providing a vast array of relevant ionospheric parameters, including neutral and ion composition and temperature, neutral wind velocity, and geopotential surface height.

Despite this, it is not the be-all-end-all, and there remains significant need for other models to fill in the gaps. TIEGCM has a minimum height of around 97 kilometers, and was designed to simulate global, not local, phenomena. Additionally, because TIEGCM is a theoretical, not empirical, model, and thus cannot possibly account for the variation caused by small-scale, localized phenomena. While LIDRM does not purport itself as being able to fill these gaps, it is hoped that our work can demonstrate the places where these gaps are most evident, and to provide background for future in-situ and remote sensing observations. In addition, little attention has been placed on the constraints of the Earth's ionospheric dynamo region–ironically, far more attention has been given to the dynamo on Mars (Riousset et al., 2013, Lillis et al., 2019) And much of the attention which has been placed on it came to erroneous conclusions, like those seen in Yi et al., 2023 (see Section IV.2).

Additionally, our understanding of global current systems is hampered by uncertainties relating to the ionospheric currents generated by dynamo forcing (the so called "solar quiet, or Sq, currents (Yamazaki & Maute, 2017)). At higher latitudes, these currents work in addition to magnetospheric-forcing driven currents to drive the polar current system (Ritter et al, 2004). Greater understanding of these currents will allow us to better constrain the geomagnetic field and assist in future modelling endeavors.

Section II.3: Sounding Rocket Assistance

This model was constructed with the intention to be used as a tool to parameterize the ionospheric conditions to constrain sounding rocket observations. Easy-to-obtain profiles of ionospheric current density and ion- and electron-neutral collision frequencies will provide future researchers with greater clarity as to the areas of greatest interest. To illustrate a use case of LIDRM, we specify a novel sounding rocket mission profile, aiming to provide high-quality measurements of ionospheric currents and neutral winds.

Current options for obtaining neutral wind speed measurements all have significant limitations. However, advancements in commercial off-the-shelf (COTS) hardware provide a potential new technique for the retrieval of upper atmospheric neutral wind velocities, first described in 2024 by Mesquita et al. This technique makes use of two different area-to-mass ratio spheres which are released from a sounding rocket before falling to the ground. Similar to the older falling sphere technique, these spheres are blown around by wind as they fall through the atmosphere. Using modern COTS GNSS receivers, the position of these spheres can be obtained to a high degree of temporal and spatial accuracy. By comparing the movement of two different area-to-mass ratio spheres, it is possible to deduce neutral wind speeds with greater precision than any other available method. Simulations show that even with deliberately large uncertainties, this novel falling sphere technique produces an average error of 1-2 m/s at 100 km–less than half that of current methods. In addition, this method provides greater accuracy in the presence of large wind shears, which can be further reduced by employing a greater number of spheres.

The relative simplicity of such a system may allow for cheaper development and production, potentially allowing for many similar missions to be performed across a variety of

locations and conditions. Currently, wind measurements in places like the upper thermosphere are poorly distributed around the globe, and modelling diverges away from observation around 200 km (Heelis & Maute, 2020). A highly accurate wind measurement technique could help to resolve these disputes, greatly enhancing our comprehension of the dynamo region.

A mission profile for such a mission may look something like this: a sounding rocket will launch with an apogee of ~150 km. A main payload will then eject four sub-payloads in two pairs, with each pair possessing a different area-to-mass ration. Each of these sub-payloads would be equipped with a high-accuracy GNSS receiver, an inertial measurement unit (IMU), a 3-axis vector magnetometer, and an electric field analyzer. The main payload should be equipped with an attitude control system, a 3-axis vector magnetometer, and command and control equipment. As they fall through the atmosphere, they transmit their data back to the main payload. All 5 sections will then be recovered via parachute at the end of their fall.

There are several existing systems that could be adapted to fit the needs of such a mission. One of these is the Swarm communications technology, developed by NASA. This system consists of a collection of ejectables, each 3.4 inches in diameter and 13.4 inches long, which are ejected from the main payload of a sounding rocket (Burth et al., 2023). While much of the payload space on the ejectables is taken up by existing systems, adapting Swarm to fit this mission would significantly simplify the design process. Additionally, the use of an existing technique for deployment of the falling sphere would also greatly simplify design and production and allow for a higher launch cadence which could provide important local information on ionospheric neutral wind velocities and electric currents.

Section II.4: Model Necessity

Currently, there exists no publicly available model capable of producing ionospheric current density profiles, or dynamo region-specific output data. Ironically, theoretical work concerning this topic has been far more active regarding the Martian ionosphere (Riousset, 2013, Yamazaki & Maute, 2016). Additionally, one of the few papers which attempts similar work we believe is significantly erroneous. The following section will discuss the theoretical basis for model we have developed to fit this purpose, which we have named the Localized Ionosphere Dynamo Region Model, hereby referred to as LIDRM.

Section III: Model Design

This section will discuss the methodology used to create LIDRM, and justify the choices made throughout the process.

Section III.1 Background

We use data from a total of four empirical and one theoretical model to obtain the background information necessary. We use the International Reference Ionosphere (IRI) the International Geomagnetic Reference Field (IGRF), the NRL's Mass Spectrometer Incoherent Scatter Model (MSIS), and the Horizontal Wind Model 2014 (HWM14) to obtain the density and temperature distributions of ionospheric particles, terrestrial magnetic field data, temperature and density distributions of neutral particles, and horizonal wind strength respectively. We also use the Average Magnetic field and Polar Current System model (AMPS) to obtain measurements of polar ionospheric currents, which are used to obtain electric currents at polar latitudes.

The IRI was developed jointly by the Committee on Space Research (COSPAR) and the International Union of Radio Science (URSI). It uses data sourced from Incoherent Scatter Radars (ISRs), ionosondes, satellite measurements, and in-situ observations to provide outputs for ion and electron density and temperature, ion composition, and several other parameters which are spurious for our model. The IRI supports custom model inputs, a functionality which we have incorporated into LIDRM.

MSIS was developed by the Naval Research Laboratory, and it combines extensive measurements of neutral species density to return a unified empirical model. It provides neutral density profiles for the seven most abundant chemical species in the upper atmosphere. The IGRF was developed by the International Association of Geomagnetism and Aeronomy, and it provides 3-dimentional magnetic field vector information for any given location and time. The

IGRF is generated by calculating a thirteen-degree expansion of spherical harmonic coefficients, using empirically measured coefficients. HWM14 provides zonal and meridional horizontal wind information, using data from satellites and ground instrumentation to provide empirical outputs of atmospheric neutral winds. Finally, AMPS is an empirical model of the polar ionosphere, using data collected from the Swarm and CHAMP satellites to model ionospheric response to magnetospheric forcing.

To develop our model in Python, we used community-published Fortan to Python wrappers to allow us to run our models in a Python environment. For MSIS we used pymsis, created by Greg Lucas. For the IRI, we used iricore created by Vadym Bidula. Finally, we used rilma's wrapper pyHWM14 and Michael Hirsh's igrf wrapper for the HWM and IGRF, respectively. We used the official pyAMPS model, provided by Karl M. Laundal. We also used another of his published projects, "Dipole" to calculate the dipole tilt needed for input into pyAMPS. Finally, we used ApexPy to convert between geomagnetic and geographic coordinate systems.

Section III.2: Model Setup

Our model is designed to require a minimum number of inputs for greater ease of use and flexibility. Given a specific date, location, and altitude range, our model is capable of generating ionospheric current, total electron density, auroral electron density, in addition to Hall and Pedersen conductivity profiles. LIDRM's first step is to obtain the parameters generated by the IRI, MSIS, and IGRF. The neutral atmosphere parameters are then used to calculate the electron-neutral and ion-neutral collision frequencies. We use the equations published in Schunk and Nagy (2000) to obtain the non-resonant collision frequencies, and we use the equations published in Ieda (2019) to obtain updated equations for resonant ion-neutral collision frequencies. We

obtain electron and ion temperatures from IRI, and species density and neutral temperatures from MSIS. For ease of calculation, LIDRM computes the average electron and ion collision frequencies to obtain the total collision frequency for both ions and electrons.

We calculate electron and ion gyrofrequency with a similar mechanism using equation 1 (in section I.2). LIDRM calculates the gyro and collision frequencies for the three most populous neutral and ionized species: N_2, O_2, O, NO^+, O^+, and O_2^+. While there are other species present, these species combine to compose the vast majority–as a result, collision frequencies between charged particles and other species are negligible and are thus ignored for our purposes.

Section III.3: Precipitation Modelling

While the IRI is capable of successfully modelling ionospheric parameters, it is primarily a climatological model, used for longer-term observation of ionospheric parameters. As a result, it can struggle to successfully model shorter-term phenomena, such as magnetospheric substorms. LIDRM attempts to account for this by using a combination of models to provide updated electron density profiles for perturbed conditions.

We first use the model developed by Hardy et al. (1987) (which will be subsequently referred to as the Hardy model) to calculate energy and number flux, as well as height-integrated Hall and Pedersen conductivities. Given a specific latitude, magnetic local time (MLT), and Kp-index, the Hardy model uses a lookup table to obtain the desired value. We can also use the total energy and number flux to calculate the average energy of the precipitating particle.

Once we have obtained data regarding the energy and number fluxes, we then use the method derived by Fang et al. (2010) to obtain a height profile of the ionization rate:

$$q_{\text{tot}}(\text{z}) = f \cdot \left(\frac{Q_{\text{mono}}}{\Delta\epsilon}\frac{1}{H(z)}\right) \tag{2}$$

Where $q_{(\mathrm{tot}}(z)$ is the ionization rate for a given altitude z, f is energy dissipation, Q_{mono} is the incident electron energy flux, H(z) is the atmospheric scale height, and delta epsilon is a constant equal to 0.035 keV. The energy dissipation is calculated from an exponential function with coefficients given by exponential of a 3rd order polynomial, calculated with the given coefficients and the incident energy. This method returns the ionization height profile for a monoenergetic electron spectra distribution.

To calculate ionization for Maxwellian and Kappa distributions, Fang et al. provides definitions of these distributions. We then used the following formula (from Bender et al., 2021) to calculate the total ionization dependent on profile:

$$q(h) = \int_0^\infty q_{\mathrm{mono}}(E,h)\phi(E)EdE \tag{3}$$

Where the phi function is based on the distribution. We then integrate this over the realistic range of energy levels to arrive at our ionization rate profile. However, it is still necessary to determine which energy profile to use. To determine this, we use a simplified version of the map developed by McIntosh & Anderson (2014). Given a location and MLT, these maps will determine which spectra is the most accurate. However, because these maps were descriptive and not prescriptive, roughly 10% of distributions were classified as "broadband"–these spectra lack a described distribution function, and as a result, we were unable to quantify these spectra in this version of LIDRM. All spectra which should have been marked broadband were therefore classified as monoenergetic, and we use the Fang et al. model to determine their ionization rates.

To determine the overall electron density due to electron precipitation, we can use the continuity equation:

$$\frac{\partial n_e}{\partial t} + \nabla \cdot (n_e \vec{v}) = q - \alpha n_e^2 \tag{4}$$

Where n_e is the electron density, $\vec{v}$ the neutral wind velocity, q the ionization rate and α the recombination rate. If we assume a steady state, we find that we have a simple formulation for the electron density: $n_e = \sqrt{q/\alpha}$. To quantify the recombination rate, we use the simple expression first described in Gledhill, 1986:

$$\alpha = 4.30 \cdot 10^6 e^{-2.42 \cdot 10^{-2} h} + 8.16 \cdot 10^{12} e^{-0.524h} \quad (5)$$

Where h is altitude in kilometers. This equation is valid between 50-150 km, perfectly sufficient for our purposes. From this, we can finally obtain the electron density due to particle precipitation–summing this with our climatological electron density profile from IRI, we obtain a far more realistic electron density profile which considers both long- and short-term variations. Using these values, we can calculate the Hall and Pedersen conductivities to a more accurate degree.

Section III.4: Current Density Profiles

Originally, we had intended to calculate ionospheric electric currents in the dynamo region via a simple method, using the following equation from Heelis & Maute (2020):

$$F = \sigma \vec{U} \times \vec{B} \quad (6)$$

Where F is the wind dynamo forcing, sigma is the ionospheric conductivity, U is the neutral wind velocity, and B is the geomagnetic field strength. However, this equation has a few issues: it only calculates the current due to the wind forcing–in reality, electric currents are generated in the dynamo region by the differential motion of ions and electrons (Sarris et al., 2023). A more physical way to represent ionospheric is to calculate this differential motion, and then use the following equation (from Sato et al., 1994) to obtain the ionospheric current density $\vec{j}$ at a given height z:

$$\vec{j}(z) = n_e(z) \cdot e \cdot \left(\overrightarrow{v_i}(z) - \overrightarrow{v_e}(z)\right) \quad (7)$$

Where e is the elemental charge, and $\overrightarrow{v_i}$ and $\overrightarrow{v_e}$ are the ion and electron velocities respectively.

Obtaining the electron velocity is rather trivial–the dynamo region is defined by the fact that the electron-neutral collision frequency is far lower than the electron gyrofrequency–as a result, the electron motion is primarily driven by $\vec{E} \times \vec{B}$ drift:

$$\overrightarrow{v_e} = \frac{\vec{E} \times \vec{B}}{B^2} \tag{8}$$

To obtain the ion velocities, we used equation 5.35 in Schunk & Nagy (2000) regarding transport in a weakly ionized plasma, which correctly describes the E-region. In this regime, ion velocity is given by:

$$\overrightarrow{v_i} = \overrightarrow{v_n} + \frac{e_i}{m_i}\left(\frac{\nu_{i-n}}{\nu_{i-n}^2 + \omega_i^2}\overrightarrow{E_\perp'} + \frac{\omega_i}{\nu_{i-n}^2 + \omega_i^2}\overrightarrow{E_\perp'} \times \vec{b}\right) \tag{9}$$

Where e_i is the ion charge, m_i is the ion mass, v_n is the neutral wind velocity, nu_in is the ion-neutral collision frequency, omega is the gyrofrequency, b is a unit vector directed along the geomagnetic field, and $\overrightarrow{E_\perp'} = \overrightarrow{E_\perp} + \overrightarrow{v_n} \times \vec{B}$.

The only values which are currently missing are the electric field measurements. While there are no models which currently provide these measurements, we can derive these values. At polar latitudes, ionospheric current flows are dominated by the magnetospheric influence. Laundal et al. (2020) describes a model of just these current flows in the aforementioned pyAMPS model. AMPS outputs the total current density from all sources–as a result, it is a useful source for determining the level of total current flow. Crucially, it allows us to use the following equation (from Weimer & Edwards, 2021, first described by Amm, 2001) to derive the electric field:

$$\overrightarrow{J_\perp} = \Sigma_P \overrightarrow{E_\perp} + \Sigma_H\left(\widehat{B_\perp} \times \overrightarrow{E_\perp}\right) \tag{10}$$

Where $\overrightarrow{J_\perp}$ is the horizontal electric current, Σ_P and Σ_H are the integrated Hall and Pedersen conductivities, and $\widehat{B_\perp}$ is the magnetic field unit vector. While this equation assumes the lack of neutral winds, due to the fact that high-latitude current flows are generally dominated by magnetospheric forcing (Maeda & Maekawa, 1972), we find the use of this equation justified.

Additionally, we operate under the assumption that the electric field is perfectly horizontal to the magnetic field–while this assumption is obviously false, it does not meaningfully affect the result above 45º N (Weimer & Edwards, 2021). Operating under this assumption will make the following aspect far simpler, as we can ignore the polarization effects. Additionally, we assume that the vertical electric field and current components are zero. This leaves us with the following:

$$\overrightarrow{E_\perp} = E_{\text{east}}\hat{\imath} + E_{\text{north}}\hat{\jmath} \tag{11}$$

$$\widehat{B_\perp} = -\hat{k} \tag{12}$$

Where the magnetic field vector is defined negative in the northern hemisphere. Computing the cross product, that leaves us with the following:

$$J_e\hat{\imath} + J_n\hat{\jmath} = \Sigma_P(E_e\hat{\imath} + E_n\hat{\jmath}) + \Sigma_H(E_n\hat{\imath} - E_e\hat{\jmath}) \tag{13}$$

From this, we get:

$$J_e = \Sigma_P E_e + \Sigma_H E_n \tag{14}$$

$$J_n = \Sigma_P E_n - \Sigma_H E_e \tag{15}$$

Solving this system of equations, we find that:

$$E_{\text{east}} = \frac{\Sigma_P \cdot J_{\text{east}} - \Sigma_H \cdot J_{\text{north}}}{\Sigma_P^2 + \Sigma_H^2} \tag{16}$$

$$E_{\text{north}} = \frac{\Sigma_P \cdot J_{\text{north}} + \Sigma_H \cdot J_{\text{east}}}{\Sigma_P^2 + \Sigma_H^2} \tag{17}$$

We can finally use these equations (in conjunction with the current density from AMPS and the integrated Hall and Pedersen conductivities from the Hardy model) to obtain an estimate of the ionospheric electric field. Finally, we can use these electric field values to calculate the ion and electron velocities, allowing us to obtain a far more accurate ionospheric current profile for polar latitudes, allowing us to quantify the specific dynamo current profile. At lower latitudes, current-induced electric fields are significantly diminished, and so the neutral-wind influenced dynamo can be approximated by the equation used by Heelis & Maute (2020). The following section will discuss the results that LIDRM is capable of producing, as well as determining where the model succeeds and fails.

Section IV: Results

We present outputs from LIDRM, and compare the outputs generated for dynamo region height and electric current density. We find that the dynamo region maintains a consistent extent from about 70 to 120 km, consistent with previous study. We also compare LIDRM's current density outputs, and compare these to the known climatological values, showing good agreement in terms of structure at all latitudes, although current densities are likely underestimated at lower latitudes.

Section IV.1: Dynamo Region Modeling

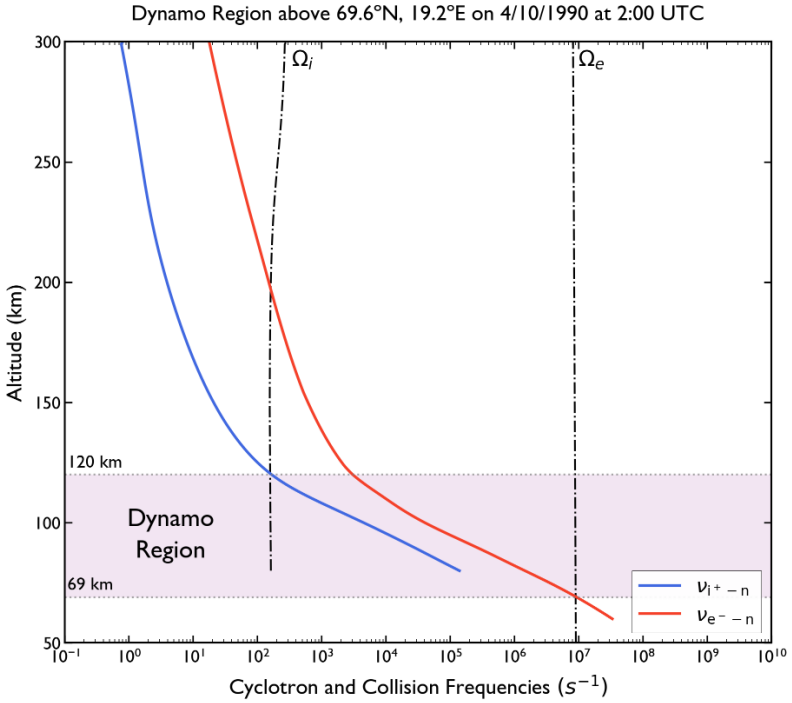


Fig. 3: Dynamo region above Tromsø, Norway

This figure shows the structure of the ionospheric dynamo region during a substorm over Tromsø, Norway on April 10, 1990, representing a typical profile for the structure of the region.

The ionospheric dynamo region occurs where electrons are magnetized (their motion is influenced by their interaction with the Earth's magnetic field), but where the ions are still

influenced by collisions with neutrals. Therefore, we defined the bottom of the dynamo region as where the electron-neutral collision frequency is higher than the electron gyrofrequency, but where the ion-neutral collision frequency is lower than the ion gyrofrequency.

We found that the dynamo region was relatively consistent across latitudes, times of day, and solar activity. This is not particularly surprising, as the collision frequencies are mostly influenced by the population of neutral particles, which remain generally consistent throughout Earths' atmosphere. We found that virtually all dynamo region profiles started from 65-72 km and ended between 115-125 km. This is consistent which much of the established literature (Lillis et al., 2019, fig 4.10 in Baumjohann and Treumann, 2022) suggests.

The height of the dynamo region seems to be primarily driven by the strength of the magnetic field–a stronger magnetic field increases the ion and electron gyrofrequencies, which mean they intersect the ion- and electron-neutral collision frequencies at lower altitudes. This feature can be seen in figure 4, which shows the dynamo region above the South Atlantic Anomaly (SAA), a region of unusually low magnetic field strength. At its weakest extent, the dynamo region stretches from 75-128 km, significantly higher than the typical dynamo region extent.

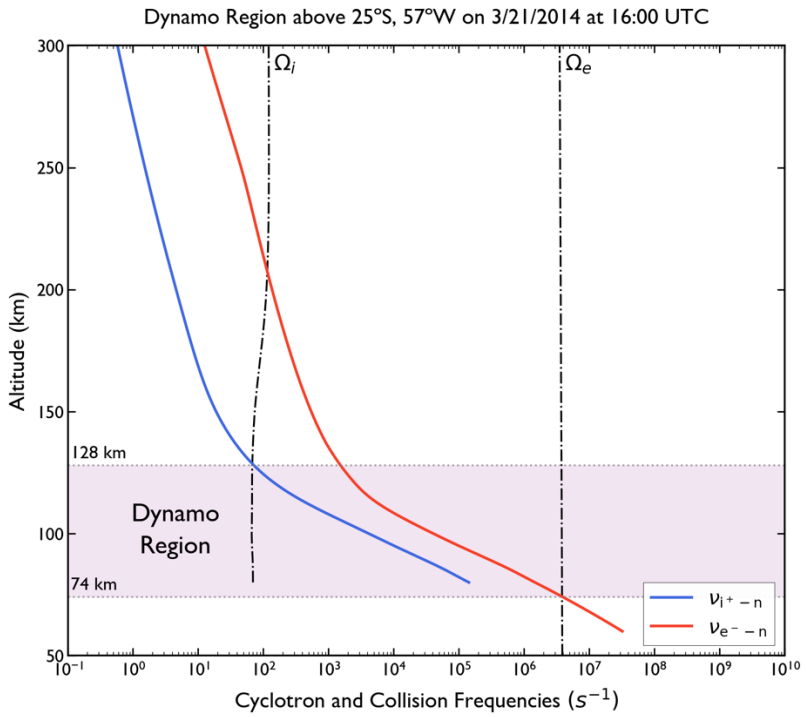


Fig. 4: Dynamo region above the South Atlantic Anomaly

The South Atlantic Anomaly is a region of unusually low magnetic field strength–as a result, the ion and electron gyrofrequencies are lower here than in the typical field strength, and so the dynamo region begins and ends at a greater altitude.

Section IV.2: Previous South Atlantic Dynamo Measurements

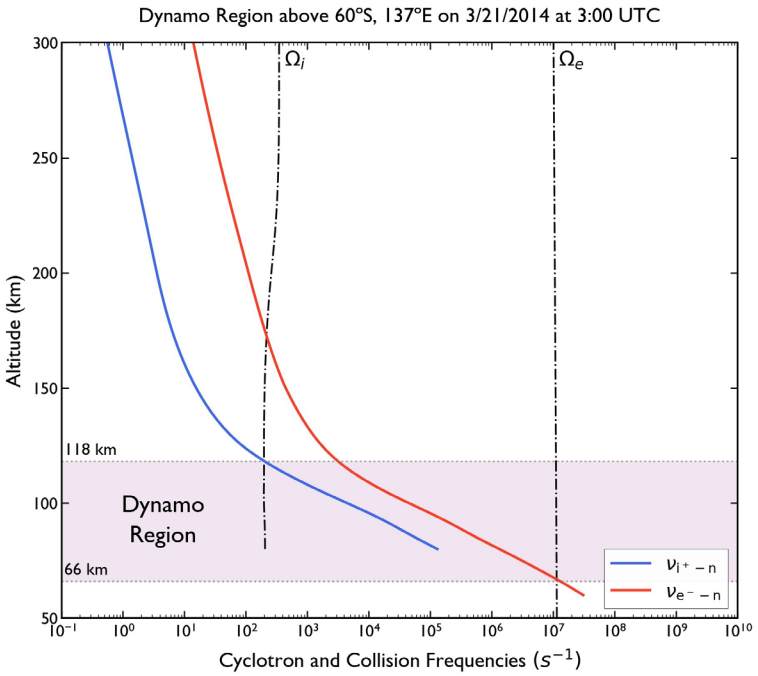


Fig. 5: Dynamo region above area of strong magnetic field

According to Yi et al., the Earths' magnetic field was strongest above 60ºS, 137ºE during their time of study. We found that the dynamo region here had a lower than typical extent, beginning at 66 km and ending at 118 km.

The above results align with what Yi et al. (2023) found in their analysis, finding that the dynamo region in the SAA was elevated compared to the dynamo region elsewhere. However, they found that the dynamo region in the SAA extended from 98 km to 218 km, and outside from 91 km to 188 km. Both of these values are well outside the expected altitude range. We allege that this is not due to a physical phenomenon, but rather a result of significant errors, which we will outline.

The paper in question, "Theoretical Study of the Ionospheric Dynamo Region inside the South Atlantic anomaly", was published in Earth and Planetary Physics (EPP) in 2023, after successfully passing peer review. While it was originally written and published in Simplified Chinese, our specific critiques concern the figures, which were all constructed in English. And while we understand that some stones are best left unturned, we will note that this paper has

received five citations to this point and is also quite prominent as a result in the Google Search algorithm. Therefore, we feel it justified in spending the time to illuminate the errors published.

The first error is relatively minor: in table 1, their footnote states that “densities are in m-3” and cites Schunk and Nagy (2018), although the formulae are identical to those in Schunk and Nagy (2000). However, the collision frequencies published in Schunk and Nagy are noted to be depicted in cm-3. This error is minor, but it potentially gives a clue as to the nature of the errors made in this paper.

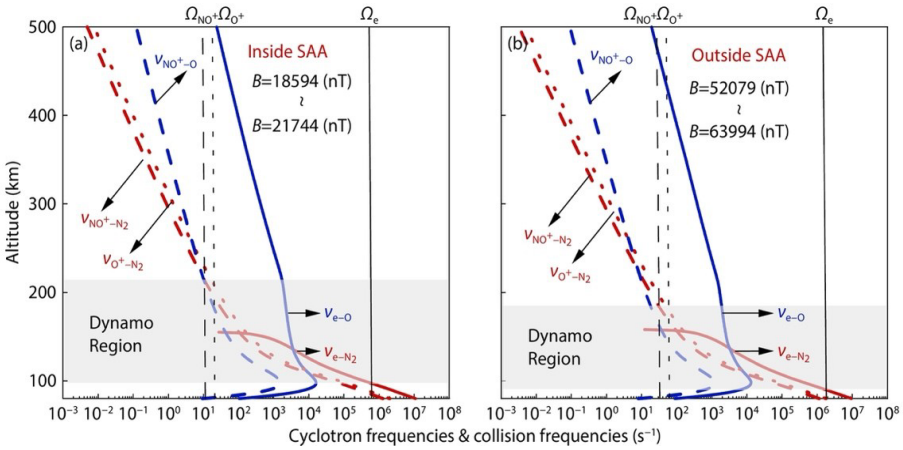


Fig. 6: Figure 2 from Xi et al., 2023

This depicts a similar plot to our figure (NUM), with collision frequencies plotted alongside ion and electron gyrofrequencies. Take note of the plot for electron-N2 collision frequency, which levels off around 160 km in altitude–something that is both unphysical, and missing from virtually every other plot of ionospheric collision frequencies.

Significant errors arise in figure 2 (fig. 6). The first and most glaring error is with the plot of the electron-N_2 collision frequency, which seems to completely level off around 160 km. This is impossible both mathematically and physically–it implies that very similar altitudes can have massively different electron-N_2 collision frequencies. Using table 1 from the same paper, we see nothing that would suggest this sort of levelling off around 160 km. In fact, table 1 shows similar

results to the ones we have plotted–this makes sense, as we both use MSIS to output our neutral densities.

To prove the mathematical impossibility of figure 2, we take specific note of the point where the electron-N2 and electron-O collision frequencies intersect–we estimated that this was around 140 km. Their figure 1 shows that the O density does not overtake the N2 density until about 180 km. Even if they were the same at 140 km (at a density of 1010 particles per cm-3), we would still expect the electron-N2 collision frequency to be significantly higher than the electron-O collision frequency. Using the exact same formulas (those from Schunk and Nagy, 2000), the electron-N2 collision frequency should be about 200 s-1, and the electron-O collision frequency should be about 44 s-1, not similar magnitudes like those depicted in their figure 2. Even at 200 km, using their own plots from figure 1, we would still expect the electron-O collision frequency to be lower.

This inconsistency is caused by the fact that while the electron-N2 collision frequency unexplainably flattens, the electron-O is about an order of magnitude higher than we would expect it to be. As for the ion collision frequency plots, these do seem reasonable, although their gyrofrequencies seem low compared to the ones we used. It seems likely, however, that they divided by an extra factor of two pi, which means their gyrofrequencies will be about one order of magnitude lower than ours.

As seen in figure 6, their findings for the dynamo region outside the SAA are inconsistent with ours as well. At the location of maximum field strength, we found that the dynamo region begins at 66 km and ends at 118 km, significantly different from what Yi et al. (2023) described. In fact, their findings for the height of the dynamo region are not corroborated anywhere else. While their conclusion–the dynamo region in the SAA is higher and larger than it is outside of it,

seems correct, their methodology and reasoning have significant deficiencies, and represent significant methodological errors on the part of the authors.

Section IV.3 Equatorial and mid-latitude current density forcing

At mid- and low latitudes, the majority of electric current forcing is due to the wind dynamo (the so-called "solar quiet", or Sq, currents) (Takeda, 2002). However, determining the relative importance of different current generation mechanisms has proven to be quite challenging (Yamazaki & Maute, 2017). We determined the magnitude of the dynamo forcing by calculating the $\vec{U} \times \vec{B}$ drift at each altitude and summing the Hall and Pedersen components to derive the total current density due to dynamo forcing. As neutral winds can exhibit significant day-to-day variability, we calculated the ionospheric current at noon local solar time every day for a year, which we then took the average to return a height density profile that represents the climatological average. While this does ignore seasonal variation, it provides a solid baseline from which to build upon.

Figure 8 depicts the average Sq current density over the Millstone Hill incoherent scatter radar, at both solar maximum (2000) and solar minimum (2019). The Solar maximum current is stronger, with a peak of $1.3 \cdot 10^{-6}$ A/m^2 at 110 km compared to the solar minimum peak current of $0.9 \cdot 10^{-6}$ A/m^2, also occurring at 110 km. These values are similar to those reported by Agodi Onwumechili (1992, II) as they observed mid-latitude currents peaking at an altitude of 112 km. Additionally, they work observed that from 7º to 35º from the magnetic equator, current densities experienced a peak value of roughly $1.6 \cdot 10^{-6}$ A/m^2. While they did not record current measurements for higher latitudes, slightly lower current densities at higher magnetic latitudes (Millstone Hill is located around a magnetic latitude of 53º N) would seems to fit our understanding.

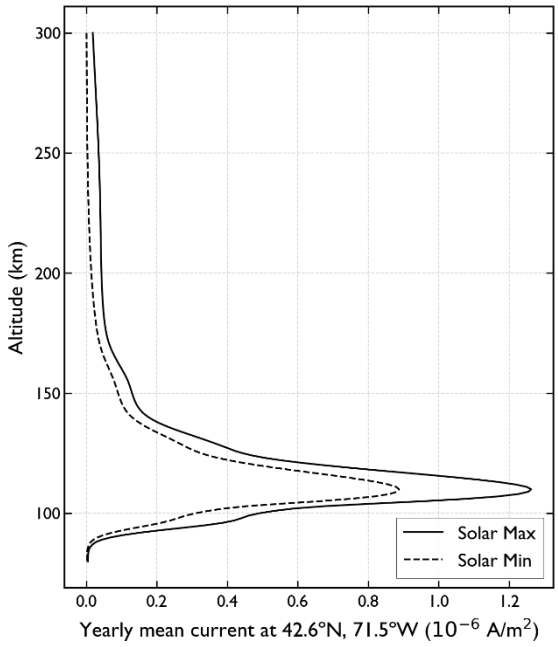


Fig. 7: Average current due to dynamo forcing above Millstone Hill, MA

Average current density due to dynamo forcing above the Millstone Hill ISR (42.6º N, 71.5º W), plotted at solar min (2019) and solar max (2000) during noon local solar time (roughly 17:00 UTC). Solar max levels are significantly elevated compared to solar min levels.

The values seen in figure 7, however, should show a greater degree of difference between solar maximum and solar minimum. Takeda (2002) found that the Sq current intensity during solar min is roughly half of the value observed during solar max, while our observations show that the current forcing is only about two-thirds of the strength. We were unable to determine what the cause of this was–the observations done by Takeda were taken over one solar cycle, whereas we used different cycles. Additionally, the halving effect may not be uniform throughout all latitudes. Further modeling work will be necessary to determine the cause of this.

Our investigation of equatorial latitudes further compounds this issue. We found that the dynamo current forcing experiences a significant *decrease* during solar max, while experiencing a significant increase during solar min.

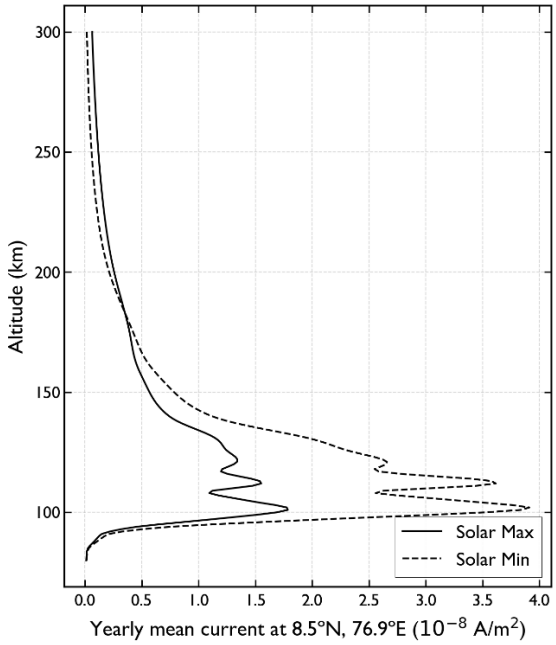


Fig. 8: Average current due to dynamo forcing above Thumba, India

Average current density due to dynamo forcing above Thumba, India (8.5º N, 76.9º E), plotted at solar min (2019) and solar max (2000) during noon local solar time (roughly 7:00 UTC). Interestingly, the solar min forcing is about three times greater than the solar max forcing.

Surprisingly, the dynamo current forcing is significantly greater during min–with a peak value of $3.9 \cdot 10^{-8}$ A/m^2 (at 101 km), compared to a solar max peak value of $1.8 \cdot 10^{-8}$ A/m^2 (at 102 km). These values are highly surprising–we would not expect the solar min current forcing to be greater than the solar max forcing, let alone more than twice as strong. Furthermore, the observed Sq current is far weaker than is typically cited along the magnetic equator. Sounding rocket experiments have found that within 0-2º of the magnetic equator (where Thumba is located), mean current densities peak at $8 \cdot 10^{-6}$, more than two orders of magnitude greater than what LIDRM retrieved (Agodi Onwumechili III, 1992).

It is likely that much of this underestimation is the fault of the simplified calculation made to find the dynamo current forcing. Our calculations ignore the Cowling effect, one of the main drivers of the equatorial electrojet (Yamazaki & Maute, 2017). It is therefore not surprising

that LIDRM underestimates the current density here. In addition to this, another possible cause of the depressed values compared to empirical observations is the lack of vertical wind data. At the magnetic equator, magnetic field vectors typically point meridionally, not vertically–as a result, the weaker vertical field will cause a weaker cross-product when it is multiplied by the zonal and meridional wind velocity. This significantly decreases the derived current forcing at lower latitudes. As a result, we find that there is very low wind dynamo forcing due to zonal and meridional winds at the magnetic equator–most of the dynamo action here is driven by the vertical movement of air masses.

However, this reasoning leaves unexplained the reversal in dynamo current intensity between solar max and solar min. Neutral wind movements are driven far more by upward propagating tides from the lower atmosphere (Yamazaki & Maute, 2017), and neutral wind structure was highly consistent between 2000 and 2019. It is therefore unclear what the root cause of the intensity reversal is, and further testing is necessary to fully explain these findings.

One of the other differences between the equatorial dynamo forcing and the mid-latitude dynamo forcing is the current structure. Close to the magnetic equator, the current density profile typically has two layers. While our profile was made in a location which was within 2º of the magnetic equator, our profile bears a greater resemblance to the profile observed 2-4º from the magnetic equator. Within 2º, the first layer experiences a peak around 105 km, with a second peak (roughly 15% as intense as the first) around 138 km. From 2-4º, the first layer still peaks at around 105 km, but the second layer peaks around 111 km. The second layer tends to be larger in magnitude than the first, although numeric averages were not given. This description fits the structure of our results far more closely. Again, it is unclear as to why this is the case, and further modeling must be done to fully explain the phenomena observed.

Section IV.4: Polar electron densities

At polar latitudes, photoionization due to solar UV radiation is no longer the dominant source of ionospheric ionization, as the effects of energetic particle precipitation (EPP) from the Earth's magnetosphere also play a significant role as an ionization source. To successfully model the current density, this precipitation must be considered.

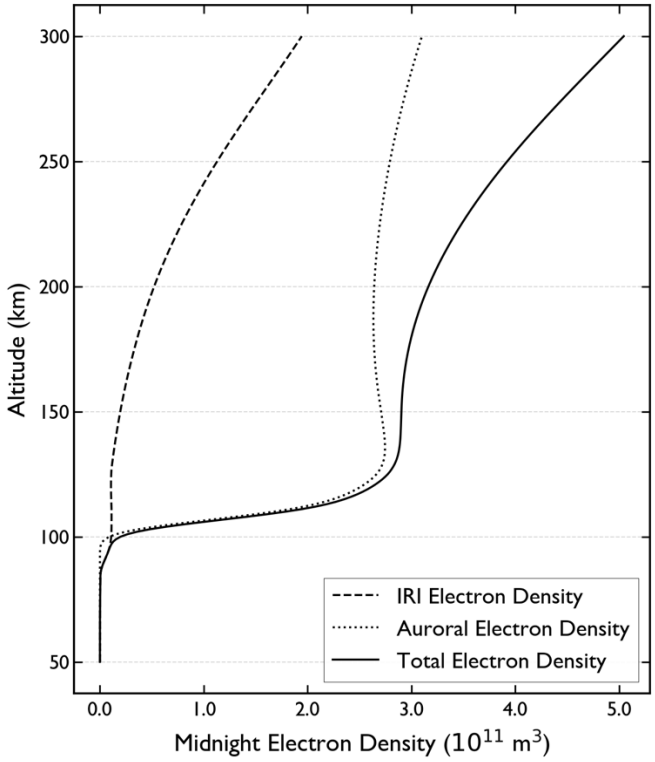


Fig. 9: Electron density at 2:00 UTC above Tromsø EISCAT ISR during substorm

Electron density profile above Tromsø EISCAT installation (69.6º N, 19.2ºE) for midnight sector (2:00 UTC) during substorm on April 10, 1990. IRI electron density is added to calculated auroral electron density to obtain total density.

Near midnight, electron density due to photoionization is very low, and so EPP is the main source of ionization. Note that while the ionization rate peaks in the E-region, the electron density increases as recombination rate decreases as density decreases. Later in the day, during

the early morning, sunlight is able to shine directly at higher altitudes, increasing the ionization rate–as can be observed in figure 10.

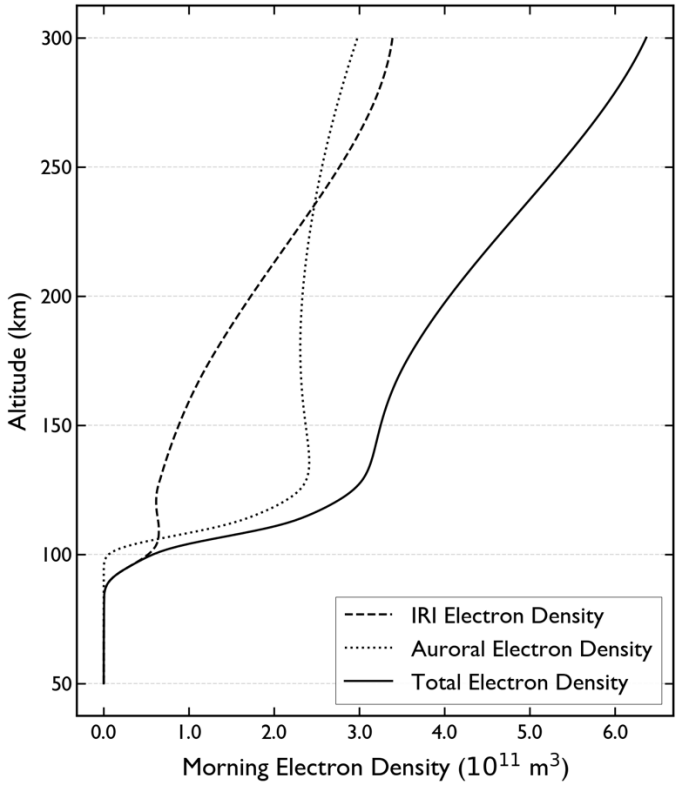


Fig. 10: Electron density at 5:00 UTC above Tromsø EISCAT ISR during substorm

Electron density profile above Tromsø EISCAT installation (69.6º N, 19.2ºE) for midnight sector (5:00 UTC) during substorm on April 10, 1990. Note the increased IRI electron density, representing increased photoionization due to solar UV.

In the early morning (5:00 UTC), increasing solar UV flux causes the IRI electron density to increase, which increases total density. Figure 11 compares the total electron density between midnight and morning. Note that the electron densities are roughly comparable until around 200 km, where the morning start pulling away due to the increased levels of photoionization.

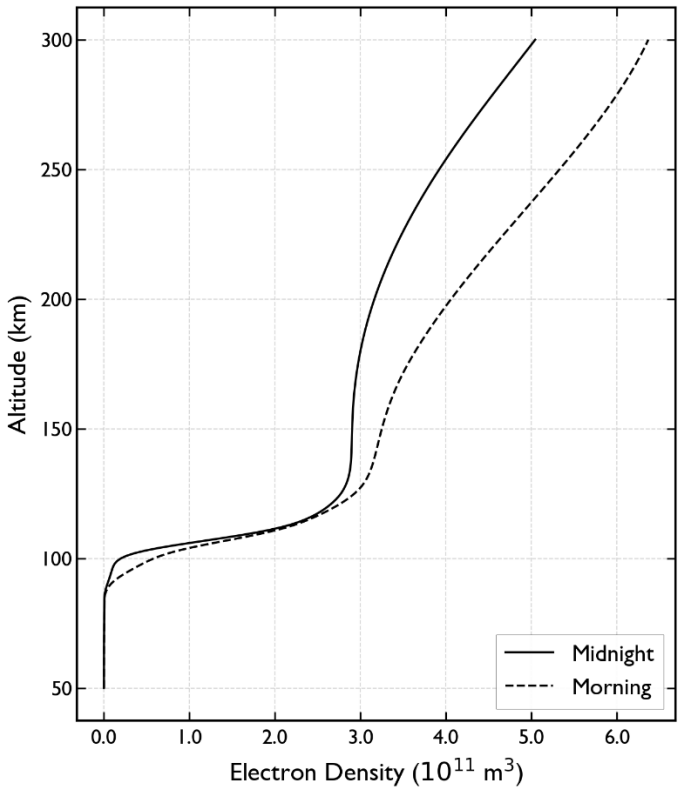


Fig. 11: Midnight (2:00 UTC) vs. morning (5:00 UTC) electron densities

Electron densities for midnight versus morning during April 10, 1990, substorm over Tromsø EISCAT installation.

Section IV.5: Polar current densities

We compared current density profiles produced by LIDRM to current density profiles derived from Tromsø EISCAT measurements from Sato et al., 1994, to determine the accuracy of LIDRMs' modeled current profiles. These measurements were conducted on April 10, 1990, during two phases: the "midnight sector", between 1-3 UTC, and the "morning sector", between 4-6 UTC. Sato et al. then averaged the measured current densities observed throughout these sectors to obtain their final current density plots, which can be seen in figure 12.

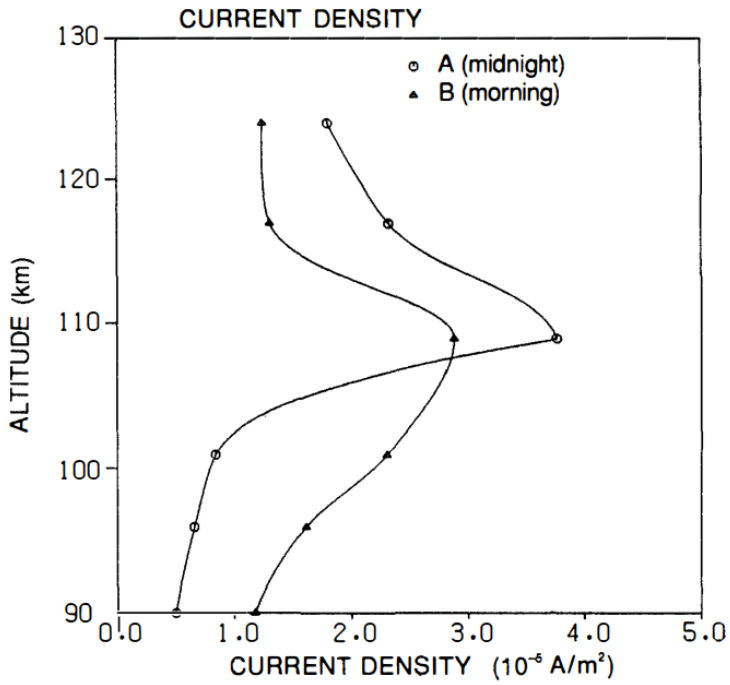


Fig. 12: Figure 2 from Sato et al., 1994

Current density observed using the EISCAT incoherent scatter radar in Tromsø, Norway, during substorm on April 10, 1990.

We can then compare this to the LIDRM outputs, shown in figure 13. Comparing just the midnight profiles, our output shows good agreement with the EISCAT values. Both have a similar peak current intensity of $4 \cdot 10^{-6}$ A/m^2 around 110 km, and a very steep increase from 100 km to the peak value. Our morning data shows worse agreement and is roughly 3 times weaker than it should be. Sato et al. note that the morning current density is greater than the midnight density until about 110 km, whereas in our model they are roughly equal. We believe this is due to issues regarding IRI modeling of dawn and dusk behavior, which can result in under/overestimations of certain output parameters. In addition, our Kp index data was incomplete during this substorm, and so the modeled Kp value is the same for both midnight and the morning sector.

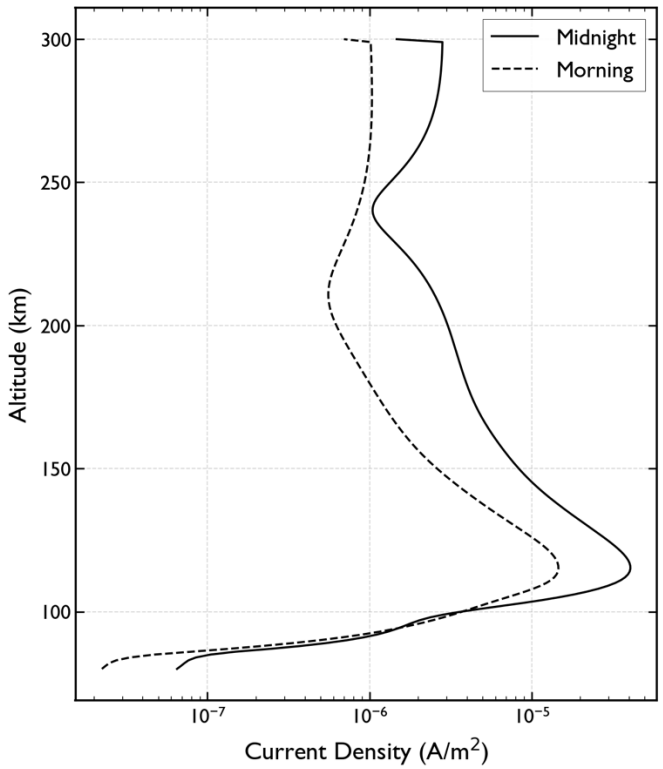


Fig. 13: LIDRM output for current density during April 10 substorm

Note the similarities between this and fig. 13 in terms of midnight density, and the differences in the morning sector current density–we should observe a greater morning density at lower altitudes.

We justify these assertations based on our Hall and Pedersen conductivity plots, shown in figure 14. Sato et al. found that at low altitudes (<100 km), the morning Hall conductivity should be roughly three times greater than the midnight Hall conductivity. To calculate the Hall conductivity, we used the following formula:

$$\sigma_H = \frac{N_e e}{B}\left(\frac{\omega_e^2}{\omega_e^2 + \nu_e^2} - \frac{\omega_i^2}{\omega_i^2 + \nu_i^2}\right)$$

Where ω and ν represent the gyrofrequency and collision frequency for ions and electrons, e is the elementary charge, B is the magnitude of the magnetic field, and N_e is the electron density. Because both runs were done on the same day within three hours of one another, it is unlikely that most of the parameters varied significantly between each LIDRM run–except for the

electron density. An underestimation of the morning electron density at lower altitudes (either from the IRI or due to greater energetic electron precipitation than expected) would lead to the low-altitude morning Hall conductivity being underestimated and therefore leading to an underestimation of the electric current density.

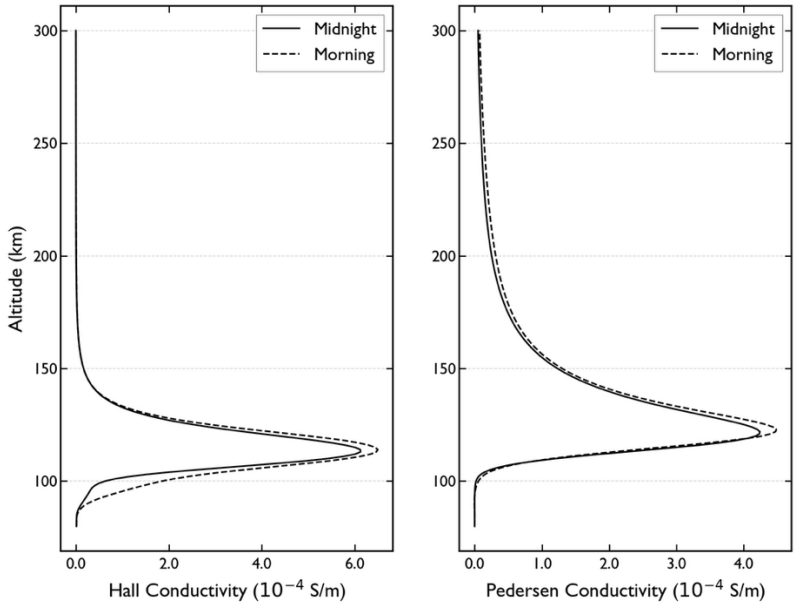


Fig. 14: Hall and Pedersen conductivity

Hall and Pedersen conductivity for midnight and morning during April 10 substorm.

Section V: Conclusions

Section V.1: Future Work

There are many opportunities for future researchers to improve upon the work that we have developed and further improve the accuracy and utility of LIDRM. There are virtually infinite directions in which this effort could be furthered, so we will take to some to specify the directions which would be most natural to take.

The most pressing concern involves improving the equatorial current density plots. Finding a model which could provide vertical wind speeds is paramount, and it would improve model accuracy over all latitudes. In addition, one could implement a similar method as we used for the polar region to estimate equatorial electric fields. Furthermore, a more advanced implementation might choose to calculate electric fields throughout the model, calculating the polarization electric fields from which current density could be resolved to a greater standard of accuracy.

Similarly, while the current method for determining polar electric fields does work, it is a very convoluted process and could do with some significant streamlining. One feature which could greatly enhance accuracy would be to use the full maps specified by McIntosh & Anderson (2014), instead of simply choosing whichever electron spectra is the strongest at a certain magnetic latitude and local time. In addition, we used a very simplified approximation for determining the electron recombination rate–a more thorough method would allow for better accuracy. Furthermore, our model lacks an option for “broadband”-type spectra, instead choosing to treat these spectra as monoenergetic. Further work should address both issues.

Because the model was optimized to produce values in the E-region, D- and F-region specific dynamics have been mostly neglected. Future improvements could include better

consideration of high and low-altitude dynamics, particularly when it pertains to ionization and recombination rates.

In addition, significant optimizations are needed throughout much of the codebase. Many operations are not vectorized and there is a significant unnecessary repetition. Further, much of the code remains messy and unorganized–class structures are inconsistent, and there are a number of unnecessary universal variables which are scarcely used. Optimization is necessary to be able to sanely run larger-scale modeling efforts in a reasonable period of time. Finally, a more standardized plotting infrastructure would greatly enhance usability, and would allow for faster and more in-depth probing of model shortcomings. While we would hope to keep this model in python, the use of a more optimized language for more intensive calculations could significantly improve calculation times.

There are a huge number of potential improvements–calculating conductivities per ion species, greater unit standardization, greater support for custom inputs–and so it is our hope that this work will continue to be iterated upon. LIDRM is capable of proving many plots which simply do not exist in the current literature, and so it is our hope that future work can continue to develop LIDRM into an even greater tool.

Section V.2: Conclusion

We have developed LIDRM, a python-based model which is able to determine ionospheric dynamo region parameters, wind dynamo forcing, Hall and Pedersen conductivities, auroral electron density, among others. We have found that LIDRM provides accurate dynamo region parameters for a given time and location, and we are able to estimate current density accurately at mid- and high latitudes. Compared to other ionospheric models which focus on the

global ionospheric structure, LIDRM provides high-resolution altitude profiles of a multitude of ionospheric parameters.

We have provided our full codebase, including all code used to create our figures as supplemental links. We have linked a guide on how to install the required packages needed to run LIDRM. We hope that this project will continue to be worked on, and it will be used to help inform and educate the next generation of researchers.

Bibliography

Agodi Onwumechili, C. (1992). A study of rocket measurements of ionospheric currents–III. Ionospheric currents at the magnetic dip equator. *Geophysical Journal International*, 108(2), 647-659. https://doi.org/10.1111/j.1365-246X.1992.tb04644.x

Agodi Onwumechili, C. (1992). A study of rocket measurements of ionospheric currents–II. Ionospheric currents outside the equatorial dip zone. *Geophysical Journal International*, 108(2), 641-646. https://doi.org/10.1111/j.1365-246X.1992.tb04644.x

Amm, O. (2001). The elementary current method for calculating ionospheric current systems from multisatellite and ground magnetometer data. *Journal of Geophysical Research, 106*(A11), 24,843-24,855. https://doi.org/10.1029/2001JA900021

Baumjohann, W., & Treumann, R. A. (2022). *Basic space plasma physics: Third edition*. World Scientific Publishing.

Bender, S., Epsy, P. J., & Paxton, L. J. (2021). Validation of SSUSI-derived auroral electron densities: comparisons to EISCAT data. *Annales Geophysicae, 39*(5), 899-910. https://doi.org/10.5194/angeo-39-899-2021

Bilitza, D., Pezzopane, M., Truhlik, V., Altadill, D., Reinisch, B. W., & Pignalberi, A. (2022). The international reference ionosphere model: A review and description of an ionospheric benchmark. *Reviews of Geophysics 60*(4). https://doi.org/10.1029/2022RG000792

Bolduc, L. (2002). GIC observations and studies in the Hydro-Québec power system. *Journal of Atmospheric and Solar-Terrestrial Physics*, 64(14), 1793-1802. https://doi.org/10.1016/S1364-6826(02)00128-1

Burth, R. H., Cathell, P. G., Edwards, D. B., Ghalib, A. H., Gsell, J. C., Hales, H. C., Haugh, H. C., & Tibbetts, B. R. (2023). *NASA sounding rockets user handbook*. National Aeronautics and Space Administration. https://sites.wff.nasa.gov/code810/files/SRHB.pdf

Chapman, S., & Lindzen, R. S. (1969). Atmospheric tides: thermal and gravitational (Vol. 15). Springer Science & Business Media.

ESA. (2020). Report for Assessment: Earth explorer 10 candidate mission Daedalus. European Space Agency, Noordwijk, The Netherlands. https://esamultimedia.esa.int/docs/EarthObservation/EE10_Daedalus_Report-for-Assessment-v1.0_13Nov2020.pdf

Fang, X., Randall, C. E., Lummerzheim, D., Wang, W., Lu, G., Solomon, S. C. & Frahm, R. A. (2010). Parameterization of monoenergetic electron impact ionization. *Geophysical Research Letters, 37*(22). https://doi.org/10.1029/2010GL045406

Fritts, D. C., & Alexander, M. J. (2003). Gravity wave dynamics and effects in the middle atmosphere. *Reviews of Geophysics*, 41(1). https://doi.org/10.1029/2001RG000106

Gledhill, J. A. (1986). The effective recombination coefficient of electrons in the ionosphere between 50 and 150 km. *Radio Science, 21*(3), 399-408. https://doi.org/10.1029/RS021i003p00399.

Hardy, D.A, Gussenhoven, M. S., & Raistrick, R. (1987). Statistical and functional representations of the pattern of auroral energy flux, number flux, and conductivity. *Journal of Geophysical Research, 92*(A11), 12,275-12,294. https://doi.org/10.1029/JA092iA11p12275

Heelis, R. A., & Maute, A. (2020). Challenges to understanding the Earth's ionosphere and thermosphere. *J. Geophys. Res. Space Physics, 125*(7). https://doi.org/10.1029/2019JA027497

Ieda, A (2019). Ion-neutral collision frequencies for calculating ionospheric conductivity. *J. Geophys. Res. Space Physics, 125*(2). https://doi.org/10.1029/2019JA027128.

Laundal, K. M., Reistad, J. P., Hatch, S. M., Moretto, T., Ohma, A., Østgaard, N., Tenfjord, P. A. R., Finlay, C. C., & Kloss, C. (2020). Time-scale dependence of solar wind-based regression models of ionospheric electrodynamics. *Scientific Reports, 10*(16406). https://doi.org/10.1038/s41598-020-73532-z

Lillis, R. J., Fillingim, M. O., Ma, Y., Gonzalez-Galindo, F., Forget, F., Johnson, C. J., Mittelholz, A., Russell, C. T., Andersson, L, & Fowler, C. M. (2019). Modeling wind-driven dynamo ionospheric dynamo currents at Mars: Expectations for InSight magnetic field measurements. *Geophysical Research Letters, 46*(10), 5083-5091. https://doi.org/10.1029/2019GL082536

Liu, H.-L. (2016). Variability and predictability of the space environment as related to lower atmosphere forcing. *Space Weather*, 14(9), 613-694. https://doi.org/10.1002/2016SW001450

LLoyd's of London and Atmospheric and Environmental Research, Inc. (2013). *Solar storm risk to the North American electrical grid*. https://assets.lloyds.com/assets/pdf-solar-storm-risk-to-the-north-american-electric-grid/1/pdf-Solar-Storm-Risk-to-the-North-American-Electric-Grid.pdf

Maeda, H. & Maekawa, K. (1973). A numerical study of polar ionospheric currents, *Planetary and Space Science, 21*(8), 1287-1300. https://doi.org/10.1016/0032-0633(73)90221-3.

Maute, A. (2017). Thermosphere-ionosphere-electrodynamics general circulation model for the ionospheric connection explorer: TIEGCM-ICON. *Space Science Review, 212*, 523-551. https://doi.org/10.1007/s11214-017-0330-3

McIntosh, R. C. & Anderson, P. C. (2014). Maps of precipitating electron spectra characterized by Maxwellian and kappa distributions. *J. Geophys. Res. Space Physics, 119*(12), 10,116-10,132. https://doi.org/10.1002/2014JA020080.

Mesquita, R., Hatch, S., Cohen, I. J., Dandenault, P. (2024). On the modernization of the falling spheres technique to measure neutral winds in the thermosphere. *ESS Open Archive.* https://essopenarchive.org/users/716388/articles/1033845-on-the-modernization-of-the-falling-spheres-technique-to-measure-neutral-winds-in-the-thermosphere?commit=e310cf8147ae0fa7c5c543419d9bc874b518899a

NASA Science Editorial Team. (2019, October 2). Earth's atmosphere: A multi-layered cake. https://science.nasa.gov/earth/earth-atmosphere/earths-atmosphere-a-multi-layered-cake/

Newell, P. T., Sotirelis, T., & Wing, S. (2009). Diffuse, monoenergetic, and broadband aurora: The global precipitation budget. *J. Geophys. Res. Space Physics, 114*(A4). https://doi.org/10.1029/2009JA014326

Palmroth, M., Grandin, M., Sarris, T., Doornbos, E., Tourgaidis, S., Aikio, A., Buchert, S., Clilverd, M. A., Dandouras, I., Heelis, R., Hoffmann, A., Ivchenko, N., Kervalishvili, G., Knudsen, D. J., Kotova, A., Liu, H.-L. Malaspina, D. A., March, G., Marchaudon, A., … , & Yamauchi, M. (2021). Lower-thermosphere-ionosphere (LTI) quantities: Current status of measuring techniques and models. Annales Geophysicae, 39(1), 189-237. https://doi.org/10.5194/angeo-39-189-2021

Papitashvili, N. E. & King, J. E. (2020). Omni hourly data [By GSM, Bz GSM, plasma flow speed, Kp*10 index]. *NASA Space Physics Data Facility*. https://doi.org/10.48322/gbpg-5r77, accessed 04/21/2026.

Pulkkinen, A., Bernabeu, E., Thomson, A., Viljanen, A., Pirjola, R., Boteler, D., Eichner, J., Cilliers, P. J., Welling, D., Savani, N. P., Weigel, R. S., Love, J. J., Balch, C., Ngwira, C. M., Crowley, G., Schultz, A., Kataoka, R., Anderson, B., Fugate, D., Simpson, J. J., & MacAlester, M. (2017). Geomagnetically induced currents: Science, engineering, and applications readiness. *Space Weather*, 15(7). https://doi.org/10.1002/2016SW001501

Richmond, A. D. (1979). Ionospheric wind dynamo theory: A review. *Journal of Geomagnetism and Geoelectricity (31),* 287-310. https://doi.org/10.5636/jgg.31.287

Riousset, J. A., Paty, C. S., Lillis, R. J., Fillingim, M. O., England, S. L., Withers, P. G., & Hale, J. P. M. (2013). Three-dimensional multifluid modelling of atmospheric electrodynamics in Mars' dynamo region. *J. Geophys. Res. Space Physics, 118,* 3647-3659. https://doi.org/10.1002/jgra.50328

Ritter, P, Lühr, H., Maus, S., & Viljanen, A. (2004). High-latitude ionospheric currents during very quiet times: Their characteristics and predictability. *Annales Geophysicae, 22,* 2001-2014. https://doi.org/10.5194/angeo-22-2001-2004

Sangalli, L., Knudsen, D. J., Larsen, M. F., Zhan, T., Pfaff, R. F., & Rowland, D. (2009). Rocket-based measurements of ion velocity, neutral wind, and electric field in the collisional transition region of the auroral ionosphere. *J. Geophys. Res. Space Physics, 114*(A4). https://doi.org/10.1029/2008JA013757

Sarris, T., Aikio, A., Buchert, S., et al. (2023). Plasma-neutral interactions in the lower thermosphere-ionosphere: The need for in situ measurements to address focused questions. *Heliophysics 2024 Decadal Whitepapers, 55*(3). https://doi.org/10.3847/25c2cfeb.ad2e5fe9

Sato, M., Kamide, Y., Brekke, A., & Nozawa, S. (1994). The altitude profile of ionospheric currents and conductivities deduced from EISCAT observations. *Upper Atmospheric Physics, 7*, 18-25.

Schunk, R. W., & Nagy, A. F. (2000). *Ionospheres–Physics, plasma physics, and chemistry.* Cambridge University Press. https://doi.org/10.1017/CBO9780511551772

Shore, R. M., Whaler K. A., Macmillan S., Beggan, C., Olsen, N., Spain, T., & Aruliah, A. (2013). Ionospheric midlatitude electric current density inferred from multiple magnetic satellites. *J. Geophys. Res. Space Physics, 118*(9), 5813-5829. https://doi.org/10.1002/jgra.50491

Takeda, M. (2002). Features of global geomagnetic Sq field from 1980 to 1990. *J. Geophys. Res. Space Physics, 107*(A9). https://doi.org/10.1029/2001JA009210

Vincent, R. A. (2015). The dynamics of the mesosphere and lower thermosphere: a brief review. *Progress in Earth and Planetary Science*, 2(4). https://doi.org/10.1186/s40645-015-0035-8

Weimer, D. & Edwards, T. (2021). Testing the electrodynamic method to derive height-integrated ionospheric conductivities. *Annales Geophysicae, 39*(1), 39-5. https://doi.org/10.5194/angeo-39-31-2021

Wu, H., Wang, W., Pham, K. H., Lin, D., Rao, N., Wiltberger, M. J., Lu, G., Wu, Q., Liu, H., Qian, L., Hsu, C., Pedatella, N. M., Vila-Pérez, J., McInerney, J. M., Richmond, A. D., Burns, A. G., Solomon, S. C., Maute, A., Sutton, E. K., Lu, X., … , & Yue, J. (2025). The NCAR-TIEGCM version 3.0. *J. Geophys. Res. Space Physics, 130*(9). https://doi.org/10.1029/2025JA034219

Yamazaki, Y., & Maute, A. (2017). Sq and EEJ–A review on the daily variation of the geomagnetic field caused by ionospheric dynamo currents. *Space Science Reviews, 206*, 299-405. https://doi.org/10.1007/s11214-016-0282-z

Yamazaki, Y., Yumoto, K., Uozomi, T., & Cardinal, M. G. (2011). Intensity variations of the equivalent Sq current system along the 210º magnetic meridian. *J. Geophys. Res. Space Physics, 116*(A10). https://doi.org/10.1029/2011JA016632

Yi, S. Q., Xu, X. J., Zhou, Z. L., Chang, Q., Wang, X., Luo, L., He, P. S., and Li, H. (2023). Theoretical study of the ionospheric dynamo region inside the South Atlantic anomaly. *Earth and Planetary Physics, 7*(1), 84-92. https://doi.org/10/26464/epp2023015

Zawdie, K. A., Drob, D. P., Siskind, D. E., & Coker, C. (2017). Calculating the absorption of HF radio waves in the ionosphere. *Radio Science, 52*(6), 767-783. https://doi.org/10.1002/2017RS006256

Code will be published to our github, at https://github.com/EliassenPalmFlux/.